



On the streamwise velocity variance in the near-wall region of turbulent flows

Sergio Pirozzoli[†]

Dipartimento di Ingegneria Meccanica e Aerospaziale, Sapienza Università di Roma, Via Eudossiana 18, 00184 Roma, Italy

(Received 2 January 2024; revised 8 May 2024; accepted 8 May 2024)

We study the behaviour of the streamwise velocity variance in turbulent wall-bounded flows using a direct numerical simulation (DNS) database of pipe flow up to friction Reynolds number $Re_\tau \approx 12000$. The analysis of the spanwise spectra in the viscous near-wall region strongly hints to the presence of an overlap layer between the inner- and the outer-scaled spectral ranges, featuring a $k_\theta^{-1+\alpha}$ decay (with k_θ the wavenumber in the azimuthal direction, and $\alpha \approx 0.18$), hence shallower than suggested by the classical formulation of the attached-eddy model. The key implication is that the contribution to the streamwise velocity variance ($\langle u^2 \rangle$) from the largest scales of motion (superstructures) slowly declines as $Re_\tau^{-\alpha}$, and the integrated inner-scaled variance follows a defect power law of the type $\langle u^2 \rangle^+ = A - B Re_\tau^{-\alpha}$, with constants A and B depending on y^+ . The DNS data very well support this behaviour, which implies that strict wall scaling is restored in the infinite-Reynolds-number limit. The extrapolated limit distribution of the streamwise velocity variance features a buffer-layer peak value of $\langle u^2 \rangle^+ \approx 12.1$, and an additional outer peak with larger magnitude. The analysis of the velocity spectra also suggests a similar behaviour of the dissipation rate of the streamwise velocity variance at the wall, which is expected to attain a limiting value of approximately 0.28, hence slightly exceeding the value 0.25 which was assumed in previous analyses (Chen & Sreenivasan, *J. Fluid Mech.*, vol. 908, 2021, R3). We have found evidence suggesting that the reduced near-wall influence of wall-attached eddies is likely linked to the formation of underlying turbulent Stokes layers.

Key words: pipe flow, turbulence simulation, turbulent boundary layers

1. Introduction

A fundamental challenge in fluid dynamics research is the identification of appropriate scaling laws for the turbulence properties. In wall turbulence, the classical scaling

[†] Email address for correspondence: sergio.pirozzoli@uniroma1.it

for the velocity fluctuations is based on the friction velocity, namely $u_\tau = (\tau_w/\rho)^{1/2}$, where τ_w is the wall shear stress, and ρ is the fluid density. Two length scales can instead be identified, namely the viscous (inner) length scale $\delta_v = \nu/u_\tau$ (with ν the fluid kinematic viscosity), and the outer length scale, say δ , connected with the global dimensions of the wall layer. This classical scenario, first envisaged by Prandtl (1925), was challenged by later experimental and numerical data (Spalart 1988; DeGraaff & Eaton 2000; Marusic 2001; Metzger & Klewicki 2001, to mention a few), which showed that the inner-scaled wall-parallel velocity variances have a clear Reynolds-number dependence. A theoretical layout to explain violations from strict inner-layer universality was set by Townsend (1976), through the so-called attached-eddy model, hereafter referred to as AEM. The model appeals to the existence of a self-similar hierarchy of eddies rooted at the wall, which, on account of the impermeability condition, can only convey wall-parallel velocity fluctuations in the wall proximity, thus retaining a footprint which manifests itself with superposition and modulation effects (Hutchins & Marusic 2007b; Mathis, Hutchins & Marusic 2009). The AEM and its subsequent extensions (Perry & Chong 1982; Perry, Henbest & Chong 1986; Perry & Marusic 1995; Marusic & Monty 2019) currently constitute the most complete theoretical framework to explain the distributions of the statistical properties in wall turbulence. One key prediction of the AEM is that the inner-scaled wall-parallel velocity variances at a fixed outer-scaled location should decrease logarithmically with the wall distance (Townsend 1976; Perry & Chong 1982; Meneveau & Marusic 2013). A weaker corollary of the model (Marusic, Baars & Hutchins 2017; Baars & Marusic 2020b) is that the inner-scaled velocity variances at fixed y^+ (hereafter, the ‘+’ superscript refers to inner normalization) in the inner part of the wall layer should increase logarithmically with Re_τ , where $Re_\tau = \delta/\delta_v = u_\tau\delta/\nu$, is the friction Reynolds number. If true, this corollary would imply that strict wall scaling is violated.

At least one potential weakness may be envisaged in applying the AEM to asymptotically high Re_τ . If the growth of the buffer-layer peak of the streamwise velocity variance were to persist indefinitely, and if the peak consistently occurred at the same position ($y^+ \approx 15$, see Sreenivasan 1989), it would lead to an increasingly high probability of instantaneous negative velocity events. This would likely alter the nature of the flow. Whereas the possibility of instantaneous velocity reversal in the viscous sublayer is known (Lenaers *et al.* 2012), it is hard to believe that this can extend to the buffer layer. In fact, an alternative scenario has been recently advocated by Chen & Sreenivasan (2021), whereby growth of the buffer-layer peak would saturate on account of a bound on the dissipation rate of the streamwise velocity variance. This would in turn imply that the wall-parallel velocity variances follow a defect power-law dependence with the wall distance, rather than logarithmic. Eventually, strict wall scaling would be restored in the limit of very high Reynolds numbers. Although the model of Chen & Sreenivasan (2021) lacks at the moment solid mathematical foundations, it nevertheless seems to comply with existing direct numerical simulation (DNS) and experimental data at least as well as the classical AEM. Hence, it has stirred the interest of the community, stimulating a number of follow-up studies (Chen & Sreenivasan 2022; Klewicki 2022; Monkewitz 2022, 2023; Hwang 2024; Nagib, Monkewitz & Sreenivasan 2024). A common conclusion drawn from those studies appears to be that discerning alternative scaling based solely on inspection of basic statistics, such as velocity variances, requires access to Reynolds numbers that are well beyond the capabilities of current and possibly future experimental and numerical approaches.

The key objective of this paper is showing that some insight into the asymptotic behaviour of turbulence in the near-wall region can in fact be achieved even with current










Flow case	L_z/R	Mesh ($N_\theta \times N_r \times N_z$)	Re_b	f	Re_τ	T/τ_t	Line style
B	15	$768 \times 96 \times 768$	17 000	0.02719	495.6	192.9	
C	15	$1792 \times 164 \times 1792$	44 000	0.02119	1132.2	50.4	
C-FY	15	$1792 \times 328 \times 1792$	44 000	0.02122	1132.2	46.1	
C-L	30	$1792 \times 164 \times 3584$	44 000	0.02119	1132.3	52.8	
C-LL	45	$1792 \times 164 \times 5376$	44 000	0.02114	1131.0	45.3	
D	15	$3072 \times 243 \times 3072$	82 500	0.01828	1972.0	45.1	
E	15	$4608 \times 327 \times 4608$	133 000	0.01657	3026.8	26.9	
F	15	$9216 \times 546 \times 9216$	285 000	0.01421	6006.4	18.2	
G	15	$18\,432 \times 1024 \times 18\,432$	612 000	0.01242	12054.5	6.99	

Table 1. Flow parameters for DNS of pipe flow. Here, R is the pipe radius, L_z is the pipe axial length, N_θ , N_r and N_z are the number of grid points in the azimuthal, radial and axial directions, respectively, $Re_b = 2Ru_b/\nu$ is the bulk Reynolds number, $f = 8\tau_w/(\rho u_b^2)$ is the friction factor, $Re_\tau = u_\tau R/\nu$ is the friction Reynolds number, T is the time interval used to collect the flow statistics and $\tau_t = R/u_\tau$ is the eddy turnover time.

day data. For this purpose, we examine the velocity spectra obtained from a newly generated DNS dataset of turbulent pipe flow, reaching Reynolds numbers up to $Re_\tau \approx 12\,000$, based on which we believe that informed extrapolation is possible.

2. The DNS database

This paper extends upon a previous publication on the subject, where Reynolds numbers up to $Re_\tau \approx 6000$ were achieved (Pirozzoli *et al.* 2021). Here, the database is enlarged and improved, by extending the time interval of previous DNS, and including a new data point at $Re_\tau \approx 12000$. A list of the flow cases is reported in table 1, which includes basic information about the computational mesh and some key parameters. The numerical algorithm is the same as in Pirozzoli *et al.* (2021), and details on the mesh resolution are provided in Appendix A. As one can see in table 1, the largest DNS has run for less than ten eddy turnover times, which is the commonly accepted limit to guarantee time convergence (Hoyas & Jiménez 2006). Nevertheless, careful examination of the time convergence according to the method of Russo & Luchini (2017) has shown that the estimated standard deviation in the prediction of the streamwise velocity variance in the range of wall distances under scrutiny here ($y^+ \leq 400$), is at most 0.6%. Uncertainty is obviously larger in the velocity spectra, for which confidence bands are provided, see e.g. figure 3. Essential details regarding the mean velocity profiles are provided in Appendix B; however, a comprehensive overview of the DNS results will be presented in future publications. Here, the emphasis is on the spectra of streamwise velocity and the associated variances.

3. Flow organization

The qualitative structure of flow case G (corresponding to $Re_\tau \approx 12\,000$) is not dissimilar to what observed in previous publications (Pirozzoli *et al.* 2021), in that the near-wall region is visually dominated by small-scale streaks whose size scales in inner units, and large-scale streaks scaling on R . This is well portrayed in figure 1, which shows the instantaneous streamwise velocity at a distance of fifteen wall units from the wall, each normalized by the corresponding root-mean-square value, at various Reynolds numbers. According to the established scenario (Hutchins & Marusic 2007a), the flow features a two-scale organization, with a large number of small-scale streaks whose typical size

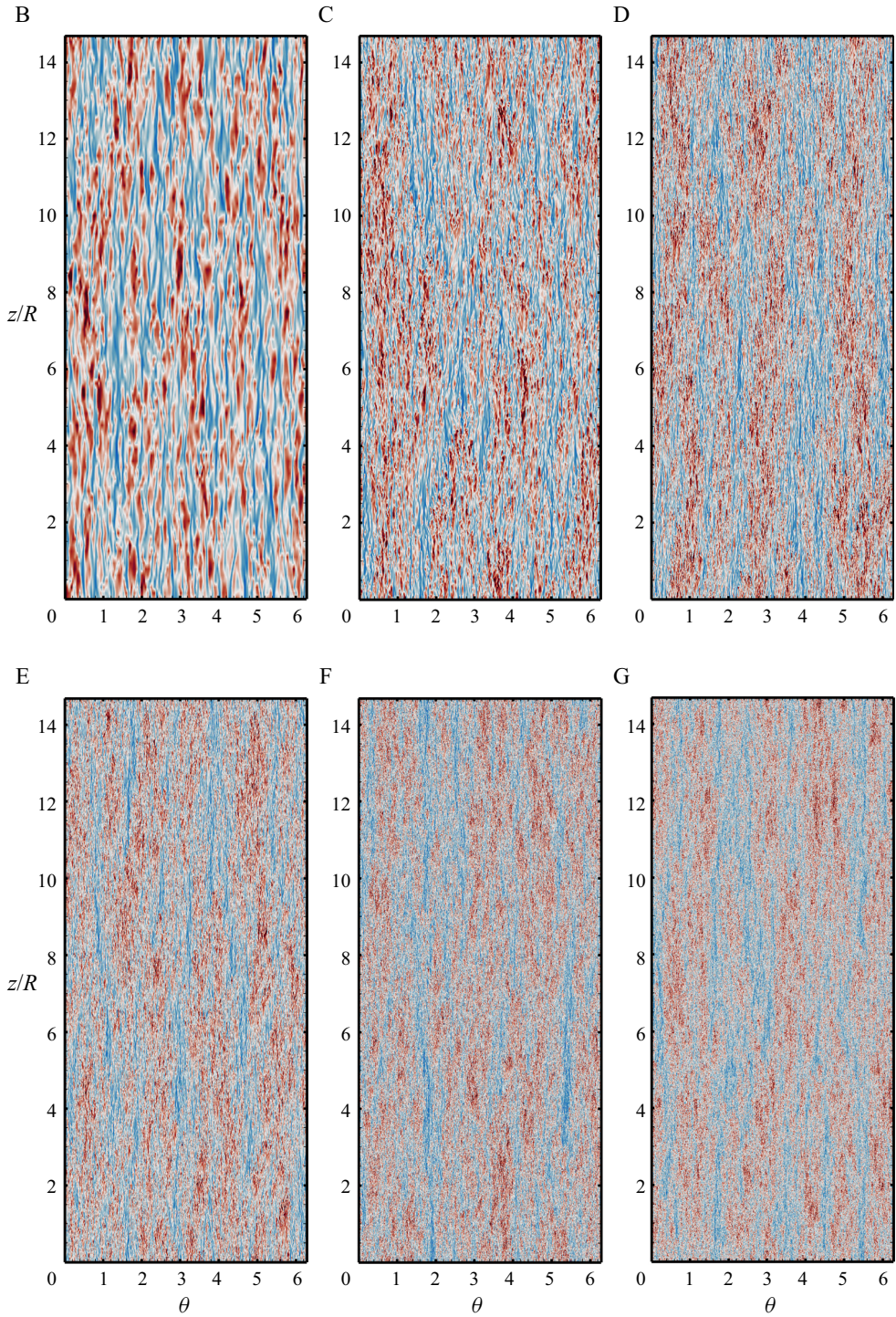


Figure 1. Normalized streamwise velocity fluctuations ($u/\sqrt{\langle u^2 \rangle}$), at $y^+ = 15$. Thirty-two contours are shown, from -3 to 3 , in colour scale from blue to red.

scales in inner units, and superposed on those large-scale streaks, being the footprint of ‘superstructures’ (according to the original definition of Hutchins & Marusic 2007a), whose size is instead proportional to R . Hence, whereas the former become vanishingly small as Re_τ increases, the size of the latter is visually unaffected. Careful inspection of the figures further suggests that the superstructures seem to be most intense at the lowest Reynolds number under consideration, whereas their strength seems to slightly decline at higher Re_τ . This observation would imply that the near-wall influence of the superstructures, which are rooted in the outer layer, slightly decreases with the Reynolds number, to an extent that we will attempt to quantify in this manuscript.

Figure 2 shows the spectral maps for the streamwise velocity field, namely the spectral densities (E_u), presented as a function of the wall distance (y) and of the spanwise wavelength (λ_θ), pre-multiplied by $k_\theta = 2\pi/\lambda_\theta$. The figure highlights the near universality of the small scales of motion, with a prominent buffer-layer peak which is universal in inner wall units, and an outer energetic site featuring R -sized very large-scale motions previously observed in experiments (Kim & Adrian 1999; Hellström & Smits 2014), and which correspond to the superstructures for the present flow. Between the two primary locations, a band of energetic intermediate modes is observed, with lengths roughly proportional to their distance from the wall, aligning with the AEM (Hwang 2015). The discrepancy between the two sites, in terms of both physical distance and of eddy size, increases in proportion to Re_τ , reaching approximately two orders of magnitude in flow case G. The figure also well clarifies that the influence of the attached eddies and of the $O(R)$ eddies on streamwise velocity fluctuations extends down to the wall. Indeed, based on dimensional arguments, spectral densities in the attached-eddy region are expected to depend on λ_θ/y , hence the corresponding iso-lines are expected to occur in bands parallel to the main energetic ridge, which we highlight with a diagonal line in panel (G). While this is approximately true in the region above the main ridge, the spectral iso-lines rather tend to attain a triangular shape in the region between the spectral ridge and the wall, as a result of energy ‘leakage’ from the overlying eddies. This region under the influence of wall-attached eddies is tentatively marked with dashed red lines in figure 2G, showing that an upper value of the wall distance exists past which the influence of outer eddies is not felt. Setting the maximum wavelength of the attached eddies to $\lambda_\theta = 0.4R$, it turns out that the maximum wall distance at which their influence is felt is $y_{max}^+ \approx 0.0044 Re_\tau$, with $y_{max}^+ \approx 530$ at the highest Reynolds number under scrutiny here. This ‘near-wall’ region is the main subject of investigation in the present study.

4. The spectra of streamwise velocity

Previous models of the velocity spectra in turbulent wall layers are mainly based on the work of Perry *et al.* (1986). The key idea is that, away from the wall, in the inviscid-dominated region, the spectra can be distinguished in three regions: the range of dissipative eddies, scaling in inner units, the region of the δ -sized eddies (here, R -sized), scaling in outer units, and a range of wall-attached eddies, for which the relevant length scale is the wall distance. In this region, under the crucial assumption that the population density of eddies that varies inversely with size and hence with distance from the wall, Perry *et al.* (1986) predicted the occurrence of a k^{-1} spectral range, where k is any wall-parallel wavenumber. Integration of the resulting spectra yields the prediction, consistent with the phenomenological theory of Townsend (1976), that the streamwise velocity variance should decay logarithmically with the outer-scaled wall distance in the region of the wall layer controlled by the attached eddies. Whereas this scenario is qualitatively confirmed in the spectral maps obtained from experiments

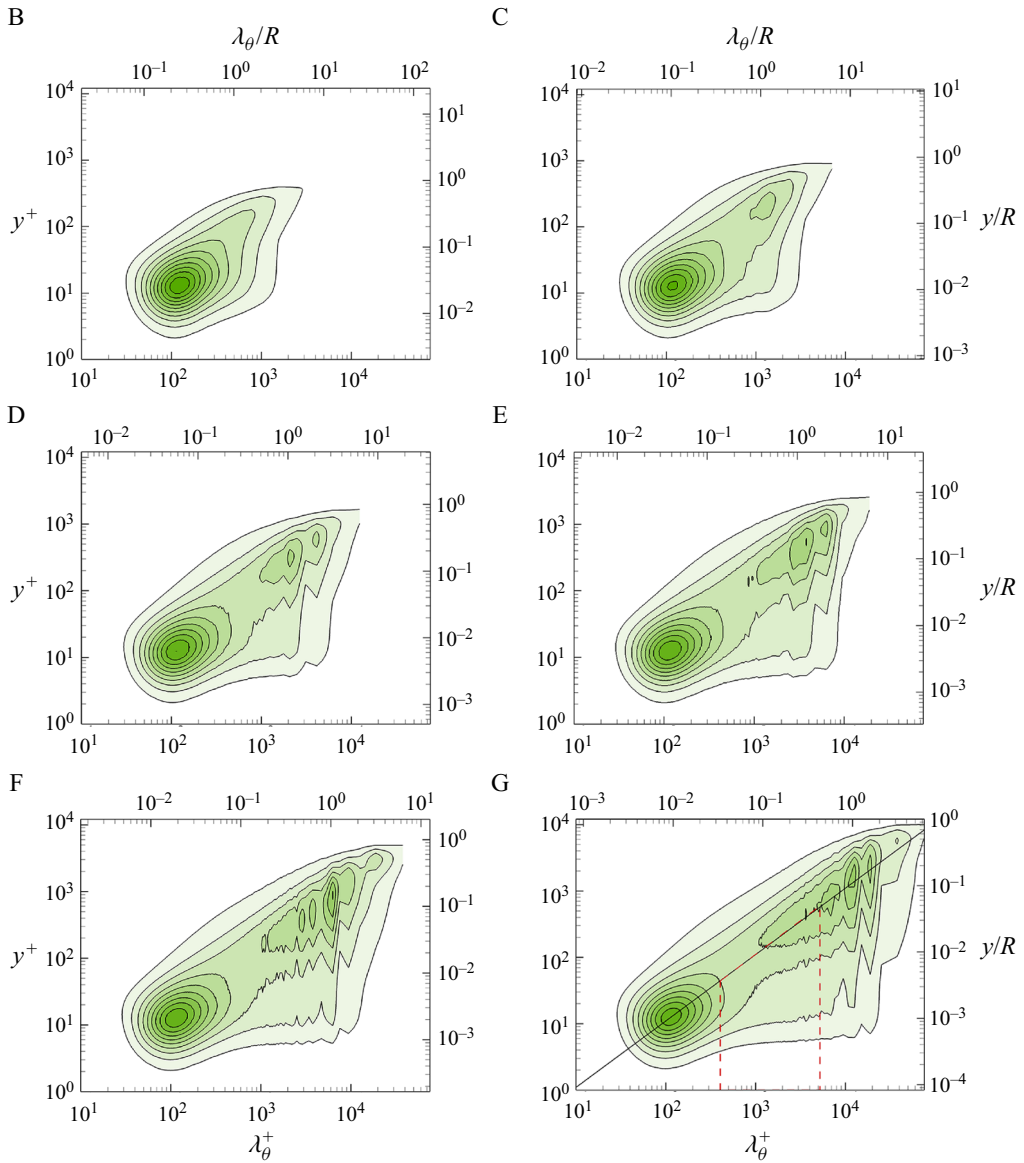


Figure 2. Variation of pre-multiplied spanwise spectral densities of fluctuating streamwise velocity with wall distance. Wall distances and wavelengths are reported both in inner units (bottom, left axes), and in outer units (top, right axes). In G the diagonal line denotes the trend $y^+ = 0.11\lambda_\theta^+$, and the trapezoidal region bounded by the red dashed line marks the region of near-wall influence of attached eddies. Contour levels from 0.36 to 3.6 are shown, in intervals of 0.36.

and DNS, quantitative evidence for the k^{-1} spectral range is quite scarce (Vallikivi, Ganapathisubramani & Smits 2015; Baars & Marusic 2020a), and the original authors (Perry *et al.* 1986) also observed deviations from the expected trend. Marusic & Monty (2019) and Baars & Marusic (2020a) noted that limited Reynolds numbers could be a reason for failure in observing the expected scaling. In any case, it is not quite clear why and how the spectral scaling in the outer, inviscid-dominated region should reflect the near-wall region in which the peak velocity variance occurs, since viscous effects

can be non-negligible (Hwang 2016). Arguments for why this should be the case were, nonetheless, offered by Marusic *et al.* (2017); Baars & Marusic (2020b).

In figure 3 we show the spanwise spectral densities of streamwise velocity fluctuations at a number of locations at fixed $y^+ < y_{max}^+$. Uncertainty bars are reported in grey shades in the left-hand side panels for flow case G, showing that the effects of limited time convergence are mainly concentrated at scales $\lambda_\theta \gtrsim R$. The figure provides clear evidence that universality of the spectra at the small scales is achieved when inner scaling is used, at least for $Re_\tau \gtrsim 2000$. Furthermore, this universal inner-scaled layer tends to become more and more extended towards longer wavelengths as Re_τ increases, until transition occurs to a R -scaled spectral range. No clear evidence for a definite k_θ^{-1} spectral range is observed, which in the pre-multiplied representation would correspond to a plateau region. Careful inspection of the velocity spectra in log–log representation (see the right-hand side panels) rather suggests the existence of a range of wavelengths with negative power-law behaviour.

Standard overlap arguments such as those used by Millikan (1938) to infer the behaviour of the mean velocity profile in wall-bounded flows can also be applied to determine the plausible structure of the velocity spectra, by assuming that: (i) the typical velocity of all eddies is the friction velocity and (ii) the typical length of the small eddies is δ_v , whereas the typical length of the large eddies is R . The transition (overlap) layer between the inner- and outer-scaled end of the velocity spectra should then have either the form of a logarithmic law, or of a power law. Based on the DNS data, the second option appears to be more appropriate, and in that case the spectral densities in the overlap layer should behave as

$$k_\theta^+ E_u^+ = C (\lambda_\theta^+)^{-\alpha} = C Re_\tau^{-\alpha} \left(\frac{\lambda_\theta}{R} \right)^{-\alpha}, \quad (4.1)$$

holding in inner and outer scaling, respectively, where α is a possibly universal constant, and C is a constant which in general could depend on y^+ . Equation (4.1) includes the k_θ^{-1} spectral scaling as a special case, occurring for $\alpha = 0$. In that case, both the small-scale end and the large-scale end of the spectrum should be universal.

The DNS data indeed support (4.1), with $\alpha \approx 0.18 \pm 0.016$, as we have estimated by fitting the DNS data for flow case G in the range of wavelengths $1000 \leq \lambda_\theta^+ \leq 10\,000$. Notably, the power-law exponent is the same at all wall distances and all Reynolds numbers, within the numerical uncertainty. The power-law range is found to be widest at $y^+ = 50$. Closer to the wall, the strong buffer-layer spectral peak tends to mask this range towards the small wavelengths, whereas farther from the wall the region under the influence of attached eddies tends to progressively shrink as y_{max}^+ is approached. This is in our opinion a very important observation, which has a number of implications.

To test the universality of the large-scale end of the spectra, in figure 4, the spectral densities are shown as a function of the outer-scaled wavelength. Universality is clearly not as good as seen for the small wavelengths in figure 3, with the energy associated with the large scales of motion becoming slightly but consistently lower at higher Reynolds number, for given λ_θ/R . In figure 5 we then show the outer-scaled spectra compensated by Re_τ^α , as suggested from (4.1). The figure shows that, with good accuracy, universality at the large-scale end of the spectrum is recovered in a wide range of scales, up to a short-wavelength limit which shifts to the left as Re_τ increases.

Overall, convincing evidence exists that the small-scale end of the velocity spectra is universal, whereas the large-scale end is not, with an overlap layer connecting the two ends which features a negative power-law behaviour with exponent $\alpha \approx 0.18$. The same

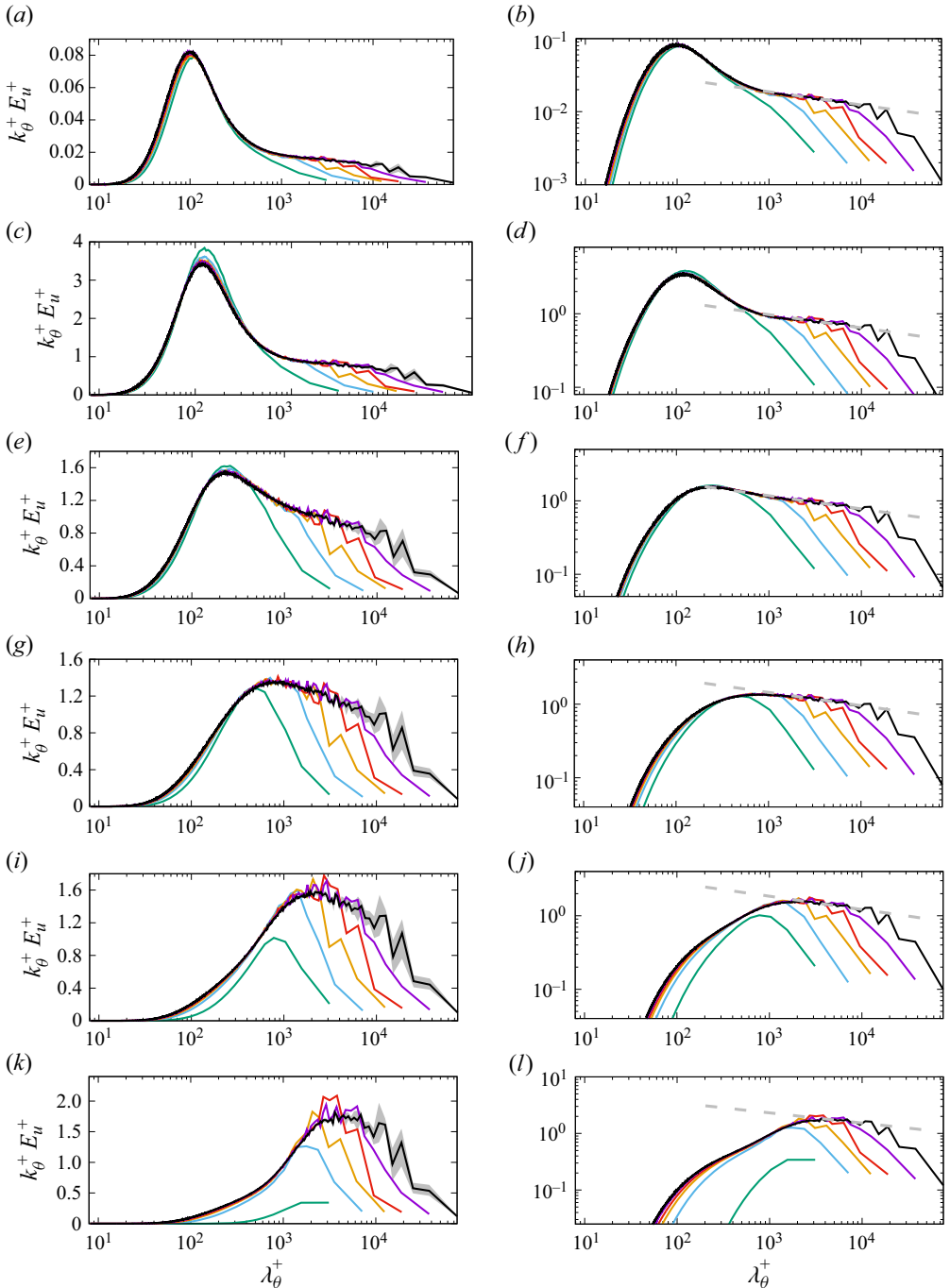


Figure 3. Pre-multiplied spanwise spectral densities of streamwise velocity at various wall distances: $y^+ = 1$ (a,b), $y^+ = 15$ (c,d), $y^+ = 50$ (e,f), $y^+ = 100$ (g,h), $y^+ = 200$ (i,j), $y^+ = 400$ (k,l). A semi-log representation is used in the left-hand side panels, and a log-log representation is used in the right-hand side panels. The shaded grey regions in the left-hand side panels denote the expected range of uncertainty for flow case G. The dashed grey lines in the right-hand side panels mark the trend $\lambda_\theta^{-0.18}$. The colour codes are as in table 1.

Streamwise velocity variance asymptotics

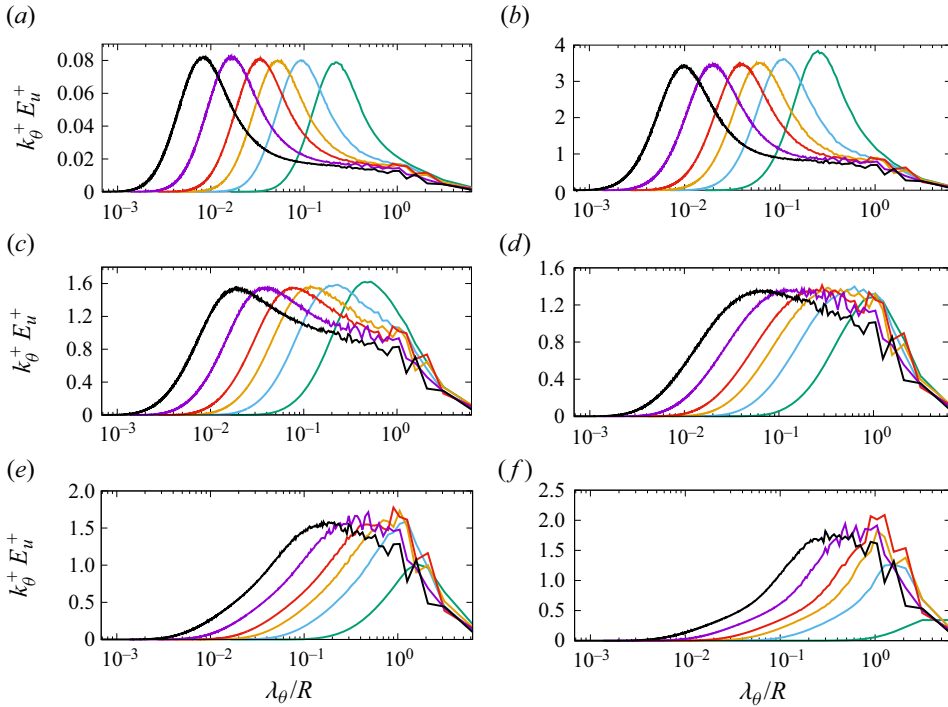


Figure 4. Pre-multiplied spanwise spectral densities of streamwise velocity at various wall distances, reported in outer scaling at $y^+ = 1$ (a), $y^+ = 15$ (b), $y^+ = 50$ (c), $y^+ = 100$ (d), $y^+ = 200$ (e), $y^+ = 400$ (f). The colour codes are as in table 1.

behaviour is also traced in spectra from plane channel flow DNS (Lee & Moser 2015), as shown in Appendix C, which corroborates the generality of our findings.

5. The streamwise velocity variance

The information derived from the analysis of the velocity spectra can be distilled to infer the behaviour of the velocity variance, taking inspiration from Hwang (2024). Letting λ_s and λ_ℓ , respectively, indicate the lower and upper limits for the observed overlap spectral range, the velocity variance can be expressed as

$$\langle u^2 \rangle^+ = \underbrace{\int_0^{\lambda_s^+} k_\theta^+ E_{u,s}^+ d \log \lambda_\theta^+}_{\langle u^2 \rangle_s^+} + \underbrace{\int_{\lambda_s^+}^{\lambda_\ell^+} k_\theta^+ E_{u,o}^+ d \log \lambda_\theta^+}_{\langle u^2 \rangle_o^+} + \underbrace{\int_{\lambda_\ell^+}^\infty k_\theta^+ E_{u,\ell}^+ d \log \lambda_\theta^+}_{\langle u^2 \rangle_\ell^+}, \quad (5.1)$$

where the subscripts s , ℓ and o denote, respectively, the contributions of the smallest scales, the largest scales and the intermediate, overlap-layer scales. Although the precise values of the limits in (5.1) are not important, it is crucial that the lower limit scales in inner units, hence $\lambda_s^+ = \text{const.}$, and that the upper limit scales in outer units, hence $\lambda_\ell/R = \text{const.}$ Based on the evidence previously given that the smallest scales tend to be universal across the Re_τ range, the associated contribution to the velocity variance is also expected to be

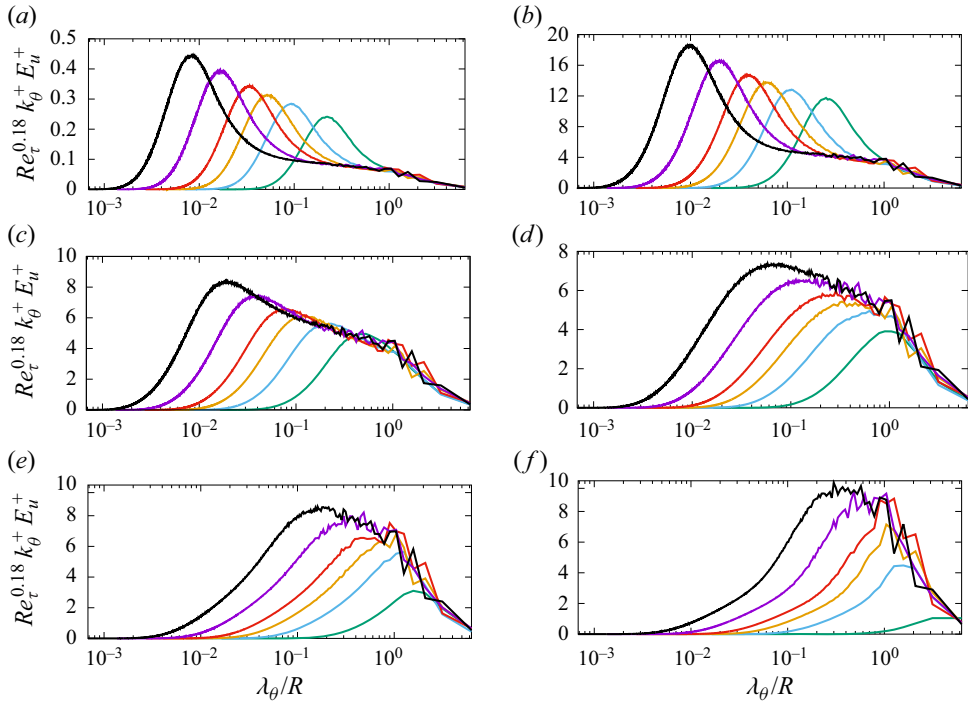


Figure 5. Pre-multiplied spanwise spectral densities of streamwise velocity at various wall distances, reported in outer scaling and compensated by $Re_\tau^{0.18}$: $y^+ = 1$ (a), $y^+ = 15$ (b), $y^+ = 50$ (c), $y^+ = 100$ (d), $y^+ = 200$ (e), $y^+ = 400$ (f). The colour codes are as in table 1.

asymptotically constant, namely

$$\langle u^2 \rangle_s^+ = A_s(y^+). \tag{5.2}$$

Since the upper end of the overlap layer should scale in outer units, we further have $\lambda_\ell^+ = Re_\tau \lambda_\ell / R \sim Re_\tau$. Based on the matching condition (4.1), and on inspection of figure 5, the contribution from the large scales is then expected to vary as

$$\langle u^2 \rangle_\ell^+ = B_\ell(y^+) Re_\tau^{-\alpha}. \tag{5.3}$$

This is an especially significant formula implying that imprinting effects imparted by the largest scales of motion (superstructures) on the near-wall region should actually decrease as Re_τ increases, in line with observations made by Hwang (2024). Last, the contribution of the overlap layer can be evaluated by integrating the power-law spectrum given in (4.1), thus obtaining

$$\langle u^2 \rangle_o^+ = \frac{C(y^+)}{\alpha} \left[(\lambda_s^+)^{-\alpha} - \left(\frac{\lambda_\ell}{R} \right)^{-\alpha} Re_\tau^{-\alpha} \right] = A_o(y^+) - B_o(y^+) Re_\tau^{-\alpha}. \tag{5.4}$$

The most important inference of the present analysis is that the overall velocity variance should then vary as

$$\langle u^2 \rangle^+ = \underbrace{(A_s(y^+) + A_o(y^+))}_{A(y^+)} - \underbrace{(B_o(y^+) - B_\ell(y^+))}_{B(y^+)} Re_\tau^{-\alpha}, \tag{5.5}$$

Station	$A(y^+)$	$B(y^+)$
$y^+ = 1$	$0.281 \pm 0.00257(0.915 \%)$	$0.396 \pm 0.0101(2.56 \%)$
$y^+ = 15$	$12.0 \pm 0.0808(0.672 \%)$	$14.2 \pm 0.319(2.25 \%)$
$y^+ = 50$	$10.6 \pm 0.105(0.985 \%)$	$20.4 \pm 0.413(2.03 \%)$
$y^+ = 100$	$11.1 \pm 0.133(1.20 \%)$	$25.2 \pm 0.526(2.09 \%)$
$y^+ = 200$	$12.3 \pm 0.185(1.51 \%)$	$31.2 \pm 0.729(1.51 \%)$
$y^+ = 400$	$13.3 \pm 0.307(2.31 \%)$	$37.8 \pm 1.21(3.21 \%)$

Table 2. Fitting parameters to use in (5.5), based on DNS data fitting, at several off-wall positions, with accompanying asymptotic standard errors ($\alpha = 0.18$ is assumed).

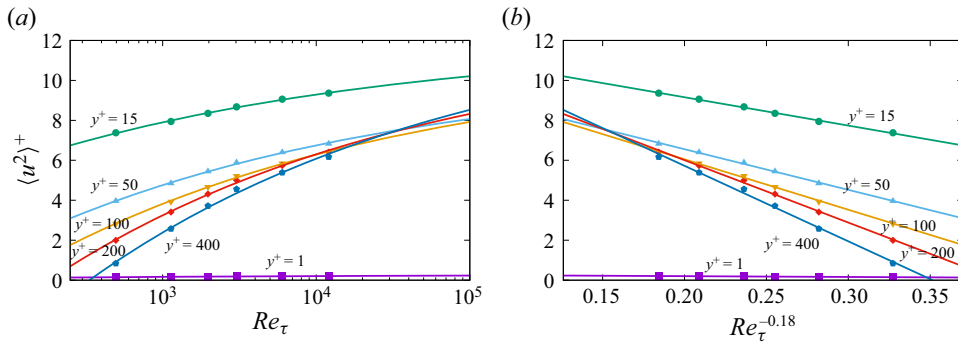


Figure 6. Streamwise velocity variances (symbols) as a function of Re_τ (a) and as a function of $Re_\tau^{-0.18}$ (b), at various off-wall positions, and corresponding fits, according to (5.5), with coefficients given in table 2.

where the functions A and B do not depend explicitly on the Reynolds number, given the assumptions made to define λ_s and λ_ℓ . Interestingly, this formula is formally identical to the asymptotic expansion suggested by Monkewitz (2022), in which $Re_\tau^{-\alpha}$ has the role of a gauge function. This formula predicts that, at any fixed y^+ , the velocity variance should increase, asymptoting to a finite limit as Re_τ increases, thus restoring strict wall scaling. Values for the asymptotic constants A, B determined from fitting the DNS data at representative off-wall locations are reported in table 2, along with the corresponding standard deviations. The resulting distributions of the streamwise velocity variances as a function of Re_τ are shown in figure 6. The quality of the fit is quite good, although it tends to deteriorate farther from the wall, since the power-law spectral range becomes narrow, making extrapolations not fully reliable. Most notably, figure 6 shows that, whereas the defect power law could well be mistaken for logarithmic growth at $y^+ = 15$, the trends at positions farther from the wall are distinctly different from logarithmic. This difference is due to the large contribution conveyed by the smallest eddies close to the wall (recalling figure 3), and tends to overshadow Reynolds-number variations associated with the larger eddies. The reduction of the energetic peak associated with the near-wall streaks occurring farther from the wall makes the actual Reynolds-number dependence manifest. Anyhow, the trend towards the asymptotic limit is quite slow, and even at as extreme Reynolds numbers as $Re_\tau = 10^6$, the predicted difference between the velocity variance at $y^+ = 15$ and its asymptotic value would still be approximately 8 %.

The extrapolated distributions of the streamwise velocity variance as a function of the wall distance are shown in figure 7, for various Re_τ . While confirming that the predictive

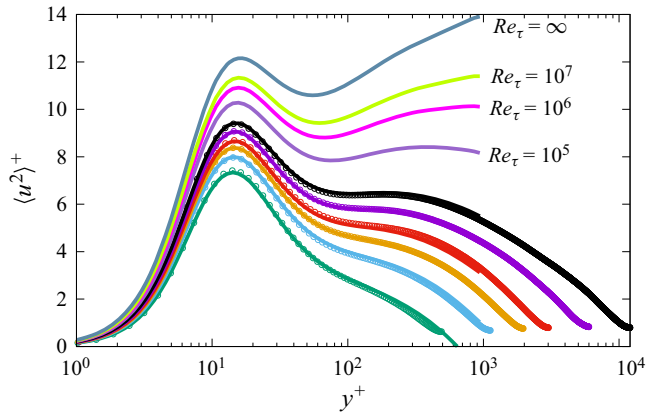


Figure 7. Predicted distributions of streamwise velocity variances at various Re_τ , according to (5.5), assuming $\alpha = 0.18$. The symbols denote the DNS data used to determine the fit coefficients $A(y^+)$, $B(y^+)$ (see table 1 for the colour codes).

formula (5.5) covers well the range of Reynolds numbers for which the model is trained, the figure also shows extrapolations beyond that range. Regarding the buffer-layer peak, it is predicted to remain more or less at the same position in inner units, and its maximum amplitude at infinite Reynolds number is predicted to be approximately 12.1. Taking into consideration the uncertainty associated with the parameter α , the buffer-layer velocity variance peak is estimated to fall within the range of 11.9 to 12.5. It is worth mentioning that these values are somewhat higher than the value of 11.5 derived from the $Re_\tau^{-0.25}$ defect law (Chen & Sreenivasan 2021), while Monkewitz (2022) obtained a value of 11.3 through an inner asymptotic expansion informed by DNS data. Farther from the wall, the distribution tends to form a shoulder as Re_τ increases, with the eventual onset of a clear ‘outer peak’. This outer peak is barely visible at the DNS-accessible Reynolds numbers, but based on the extrapolated data it should attain a higher value than the inner peak at extreme Re_τ .

The primary inquiry revolves around whether the extrapolated distributions agree with experimental measurements. To address this question, in figure 8 we present experimental data collected from various facilities using different measurement techniques. Specifically, particle-image velocimetry (PIV) measurements from the CICLoPE facility (Willert *et al.* 2017), hot-wire anemometry (HWA) measurements conducted with nanoscale thermal anemometry probes at Princeton’s Superpipe facility (Hultmark *et al.* 2012) and laser Doppler velocimetry (LDV) measurements carried out at the Hi-Reff facility in Japan (Ono *et al.* 2023) are included. The comparison reveals highly favourable agreement with all measurements at ‘low’ Reynolds numbers, approximately $Re_\tau \lesssim 5000$. However, notable discrepancies arise at higher Reynolds numbers, varying considerably depending on the set of measurements. Specifically, while alignment remains nearly perfect with the PIV measurements in the CICLoPE facility, the DNS-based extrapolations yield values significantly higher than those obtained from the SuperPipe data. A similar trend of over-prediction of the experimental data is also noticeable, albeit to a lesser degree, when comparing with the LDV measurements in Hi-Reff. In principle, these differences could arise from shortcomings in the DNS and/or its application for extrapolations, but they are more likely associated with issues in the experimental data. Indeed, the three sets of measurements utilized here for reference demonstrate notable discrepancies among each

Streamwise velocity variance asymptotics

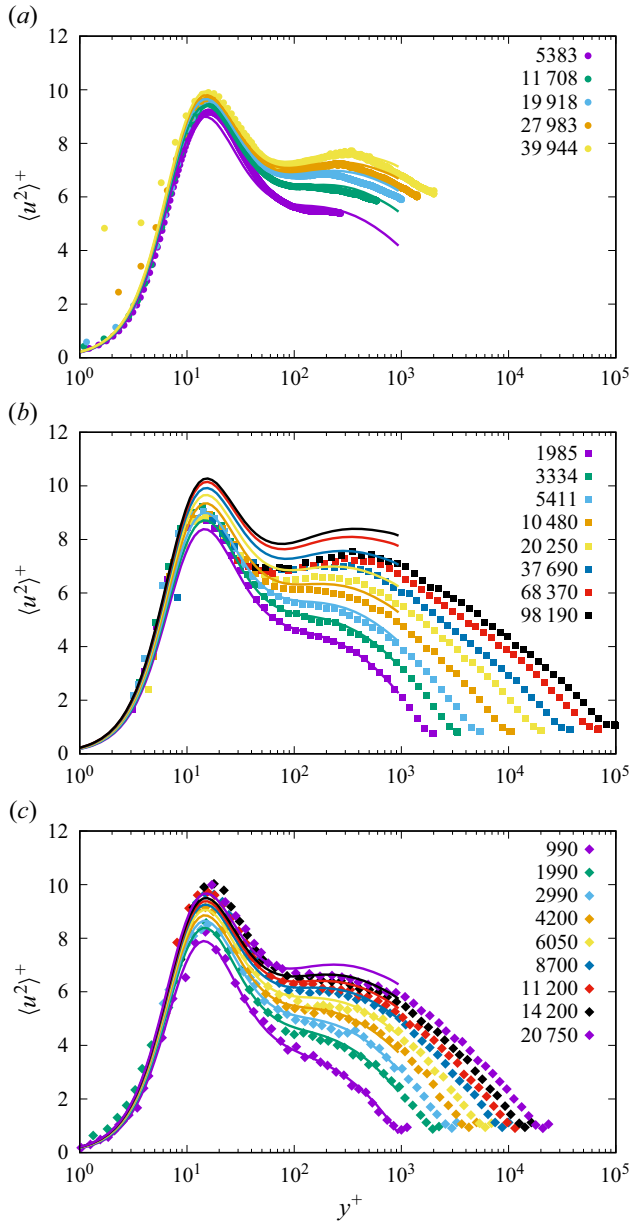


Figure 8. Comparison of streamwise velocity variance distributions predicted from (5.5) (solid lines), with experimental measurements taken at the SuperPipe facility ((b) Hultmark *et al.* 2012), at the CiLoPE facility ((c) Willert *et al.* 2017) and at the Hi-Reff facility ((d) Ono, Furuichi & Tsuji 2023), at matching values of Re_τ , as given in the respective legends.

other, suggesting possible filtering effects, particularly for HWA and LDV measurements, whereas PIV measurements might be less affected.

The current analysis also has direct implications for the dissipation rate of the streamwise velocity variance, $\epsilon_{11} = \nu \langle |\nabla u|^2 \rangle$. As noted by Chen & Sreenivasan (2021), at the wall this quantity equals the viscous diffusion term, which in inner units

is $d^2\langle u^2 \rangle^+ / dy^{+2}$. The latter quantity (not shown) is virtually indistinguishable from $\langle u^2 \rangle^+(y^+ = 1)$, since $d\langle u^2 \rangle^+ / dy^+ = 0$ at the wall. The inferred trend of $\langle u^2 \rangle^+(y^+ = 1)$ (see [table 2](#)) then implies that the wall dissipation rate should asymptote to a value of approximately 0.28, with uncertainty of ± 0.01 on account of variability of α . Although a bit higher than the upper bound of 0.25 advocated by [Chen & Sreenivasan \(2021\)](#), and the value of 0.26 predicted by [Monkewitz & Nagib \(2015\)](#) for zero-pressure-gradient boundary layers, this result suggests that wall dissipation retains the same order of magnitude as the maximum production in the buffer layer.

6. Discussion and conclusions

The current analysis, informed by spectral DNS data of turbulent pipe flow up to $Re_\tau \approx 12\,000$, raises several significant points. Firstly, it offers quantitative arguments, alongside physical intuition, suggesting that strict wall scaling should be restored in the limit of infinite Reynolds numbers. This assertion aligns with propositions put forth in recent literature ([Chen & Sreenivasan 2021](#); [Monkewitz 2022](#)), albeit founded on entirely different arguments. In particular, consistent with the assumptions made by [Chen & Sreenivasan \(2021\)](#), it appears that the appropriate asymptotic behaviour towards the infinite-Reynolds-number limit follows a defect power law. However, the exponent of this negative power law appears to deviate somewhat from the $\alpha = 0.25$ advocated in those studies, being instead closer to $\alpha = 0.18$, with an uncertainty of approximately $\pm 10\%$, as revealed by the analysis of the velocity spectra. This discrepancy might stem from the inaccurate assumption made by those authors that the wall dissipation rate should asymptotically approach 0.25 not to exceed the maximum production rate, although this assertion cannot be rigorously justified on mathematical grounds.

The current analysis fits well within the framework of the classical attached-eddy model. Indeed, the spectrograms reported in [figure 2](#) bear the clear signature of a hierarchy of wall-attached eddies. However, in contrast to the classical formulation of the AEM, we observe that the near-wall signature of these attached eddies becomes fainter as their centre moves away from the wall. This phenomenon is reflected in a spectral decay that is shallower than the traditionally accepted k^{-1} spectrum derived from inviscid arguments. A secondary implication is that the imprinting of superstructures (here, R -sized eddies) on the wall diminishes as Re_τ increases. However, this observation does not imply that inner-/outer-layer interactions are negligible. Rather, the slow decay rate implies that the influence of outer-layer eddies remains substantial at any reasonably high Reynolds number.

The crucial question revolves around the reason for the spectral slope being less steep than k^{-1} . A plausible explanation is the presence of viscous effects, which impede the flow in the near-wall region. While the AEM treats inactive motions (whose size significantly exceeds the distance from the wall) as satisfying a slip condition at the wall, in reality, they do not. In this regard, the analysis conducted by [Spalart \(1988\)](#) holds considerable merit. He argued that inactive eddies influence the near-wall region by inducing periodic, low-frequency sloshing motions, leading to the formation of Stokes layers of either laminar or turbulent nature. In the first case, analytical solution of the Navier–Stokes equations with time-periodic change of the free-stream velocity would yield the following form of the streamwise velocity variance ([Schlichting & Gersten 2000](#)):

$$\langle u^2 \rangle^+ \sim 1 + e^{-2y/\Delta} - 2 \cos(y/\Delta) e^{-y/\Delta}, \quad (6.1)$$

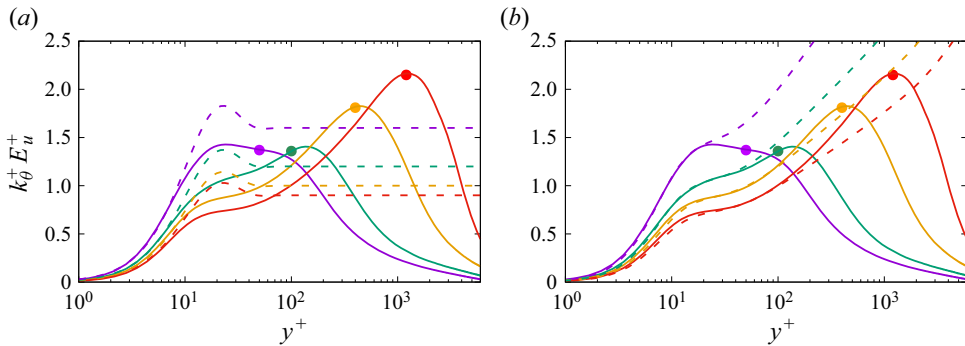


Figure 9. Flow case G: pre-multiplied spectral density of streamwise velocity as a function of wall distance, corresponding to various wavelengths: $\lambda_\theta^+ = 455$ ($y_s^+ = 50$) (purple), $\lambda_\theta^+ = 909$ ($y_s^+ = 100$) (green), $\lambda_\theta^+ = 3636$ ($y_s^+ = 400$) (orange), $\lambda_\theta^+ = 10970$ ($y_s^+ = 1205$) (red). The bullets denote the wall distance of the corresponding eddy centres, see figure 2. The dashed lines in (a) denote predictions of (6.1) with $\Delta^+ = 10$, and in (b) predictions of (6.2).

with $\Delta = (2\nu/\omega)^{1/2}$ the thickness of the Stokes layer, and ω the oscillation frequency. Bradshaw (1967) proposed a model for turbulent Stokes layers based on the idea that the primary effect of low-frequency inactive motions is a time-periodic change of the wall shear stress, namely $\tau_w = \bar{\tau}_w(1 + A \cos(\omega t))$, with $A \ll 1$. Assuming next that the law-of-the-wall has time to adapt to low-frequency modulation of the wall shear stress results in the following prediction for the velocity variance associated with inactive motions:

$$\langle u^2 \rangle^+ \sim \left(U^+ + y^+ \frac{dU^+}{dy^+} \right)^2. \tag{6.2}$$

These concepts were put to the test by Spalart (1988), who compared the predictions in (6.1) and (6.2) with the difference in velocity variances at two modest Reynolds numbers, which he used as a proxy for the contribution of inactive motions. Here, both approaches are examined by plotting profiles of $E_u^+(\lambda_\theta^+, y^+)$ for various values of λ_θ^+ , which in the AEM interpretation characterize the intensity of streamwise velocity fluctuations induced by attached eddies centred at a wall distance $y_s^+ \approx 0.11\lambda_\theta^+$ (refer to figure 2).

Figure 9(a) presents a comparison of the spectral density profiles with the prediction given by (6.1), where we have arbitrarily assumed $\Delta^+ = 10$, and attempted to adjust the slope of the DNS data at the wall. While the values of the velocity intensities appear reasonable, the shape is evidently incompatible with the DNS data. On the other hand, figure 9(b) depicts the predictions of (6.2), again after adjusting the near-wall slope. In this case, the agreement with the DNS data is remarkable, particularly for wall distances smaller than the centre of the attached eddies (indicated with bullets in the figure). This observation serves as plausible evidence that turbulent Stokes layers do indeed exist, thereby providing the retardation effects responsible for attenuating the influence of wall-distant eddies.

Although extrapolation is known to be a dangerous, oftentimes ill-posed exercise, we believe that the present observations lay down a sufficiently solid background to project today’s DNS results to much higher Reynolds number than feasible in the near or even foreseeable future. When pushed to the extreme, extrapolation of the present data would suggest a scenario where the buffer-layer peak of the streamwise velocity variance, while remaining finite, would be much larger than in any current DNS and experiments, but

roughly at the same inner-scaled position. Another important feature which we foresee is a secondary distinct peak farther from the wall, whose strength becomes comparable to and eventually larger than the buffer-layer peak. The primary caution we emphasize is that these predictions rely on the assumption that the observed expansion of the power-law spectrum will persist indefinitely. Should a definite k^{-1} spectral range arise at higher Reynolds numbers than those achieved thus far in DNS, as suggested by some experimental studies (Baars & Marusic 2020a), a logarithmic increasing trend would resume. Furthermore, it is important to highlight that the current analysis does not offer an explanation for the specific value of the spectral scaling exponent in the overlap layer. In contrast, Chen & Sreenivasan (2021) rationalized the presence of a -0.25 exponent in the proposed defect power law by attributing it to the flux of additional energy dissipation from the near-wall region to the outer flow. Thus, further theoretical efforts are still necessary to fully elucidate the observed data and unambiguously establish the asymptotic state of wall turbulence.

Supplementary movie. Supplementary movie is available at <https://doi.org/10.1017/jfm.2024.467>.

Acknowledgements. Discussions with Y. Hwang, P. Monkewitz, J. Jimenez, A.J. Smits and T. Wei are gratefully appreciated. I acknowledge that the results reported in this paper have been achieved using the EuroHPC Research Infrastructure resource LEONARDO based at CINECA, Casalecchio di Reno, Italy, under a LEAP grant. Constructive criticisms from the anonymous referees are also gratefully acknowledged.

Funding. This research received no specific grant from any funding agency, commercial or not-for-profit sectors.

Declaration of interests. The author reports no conflict of interest.

Data availability statement. The data that support the findings of this study are openly available at the web page <http://newton.dma.uniroma1.it/database/>.

Author ORCID.

 Sergio Pirozzoli <https://orcid.org/0000-0002-7160-3023>.

Appendix A. Box and grid sensitivity analysis

The grid resolution in the axial and azimuthal directions is decided based on previous experience with second-order finite-difference solvers which indicates that grid-independent results are obtained provided $\Delta x^+ \approx 10$, $R^+ \Delta \theta \approx 4.1$ (Pirozzoli *et al.* 2021), hence the associated number of grid points is selected as $N_z \approx L_z/R \times Re_\tau/10$, $N_\theta \sim 2\pi \times Re_\tau/4.1$. The wall-normal distribution of the grid points is designed after the prescriptions set by Pirozzoli & Orlandi (2021), to resolve the steep near-wall velocity gradients and the local Kolmogorov scale away from the wall, according to

$$y^+(j) = \frac{1}{1 + (j/j_b)^2} \left[\Delta y_w^+ j + \left(\frac{3}{4} \alpha c_\eta j \right)^{4/3} (j/j_b)^2 \right], \quad (\text{A1})$$

where $\Delta y_w^+ = 0.05$ is the wall distance of the first grid point, $j_b = 40$ defines the grid index at which transition between the near-wall and the outer mesh stretching takes place and $c_\eta = 0.8$ guarantees resolution of wavenumbers up to $k_{max}\eta = 1.5$, with η the local Kolmogorov length scale. The distributions of the grid points for the DNS listed in table 1 are shown in figure 10(a). A slightly finer mesh is used for flow case G than for the other cases. The wall-normal resolution is verified *a posteriori* in figure 10(b), where we show the grid spacing expressed in local Kolmogorov units, which is found to be no larger than 2.2 throughout the radial direction.

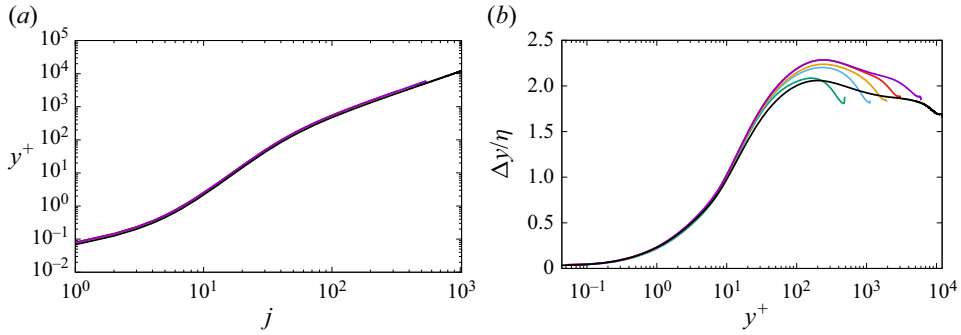


Figure 10. (a) Distribution of wall-normal grid coordinates as a function of grid index (j), and (b) corresponding grid spacings expressed in Kolmogorov units. The colour codes are as in table 1.

The sensitivity of the computed results to the computational box size and grid resolution has been assessed through additional simulations conducted at $Re_b = 44\,000$ (flow case C), as listed in table 1. Specifically, we have doubled the number of points in the radial direction (flow case C-FY) and doubled and tripled the pipe length (flow cases C-L and C-LL, respectively). All these flow cases have been simulated for numerous eddy turnover times, for the purpose of removing the time sampling error. The resulting change in the one-point statistics is well below 1%, as illustrated in figure 11, even for flow properties that are challenging to converge over time, such as the log-law indicator function (Hoyas *et al.* 2024). Figure 12 additionally presents a comparison of the pre-multiplied spanwise spectra at several off-wall positions for the same flow cases. Once again, box and grid independence is demonstrated to be excellent, indicating that uncertainties primarily stem from finite time sampling.

Appendix B. Mean velocity profiles

The mean velocity profiles for the DNS cases listed in table 1 are presented in figure 13(a), accompanied by the associated log-law diagnostic functions shown in panel (b). The latter quantity is commonly used to verify the presence of a genuine logarithmic layer in the mean velocity profile, which would be indicated by a plateau. This diagnostic function exhibits two peaks: one corresponding to the buffer layer, which is nearly universal in inner scaling at $Re_\tau \gtrsim 10^3$, and an outer peak corresponding to the wake region, which also becomes approximately universal in inner units. Between these two regions, the distribution tends to change significantly with the Reynolds number. While previous DNS and analyses suggested linear deviations from the logarithmic behaviour (Afzal & Yajnik 1973; Jiménez & Moser 2007; Luchini 2017; Pirozzoli *et al.* 2021), at the highest Reynolds number achieved in this study, the onset of a genuine logarithmic layer is observed, starting at $y^+ \approx 500$ and extending up to $y/R \approx 0.2$. This finding is consistent with the SuperPipe data (symbols in panel (b)), recent DNS of plane channel flow (Hoyas *et al.* 2022) and is in line with the theoretical analysis of Monkewitz (2021). The data support a value of the Kármán constant of $\kappa \approx 0.38$, slightly less than estimated in previous studies, in which, however, a genuine logarithmic layer was not observed. The figure reveals a large scatter associated with limited time convergence of flow case D for this indicator, confirming recent analyses (Hoyas *et al.* 2024). While the predictions for the inner layer appear to be robust, much longer integration times are required to achieve satisfactory convergence of statistics associated with velocity derivatives. However, achieving such convergence is currently beyond the capabilities of DNS. Figure 13(a) confirms that the mean velocity

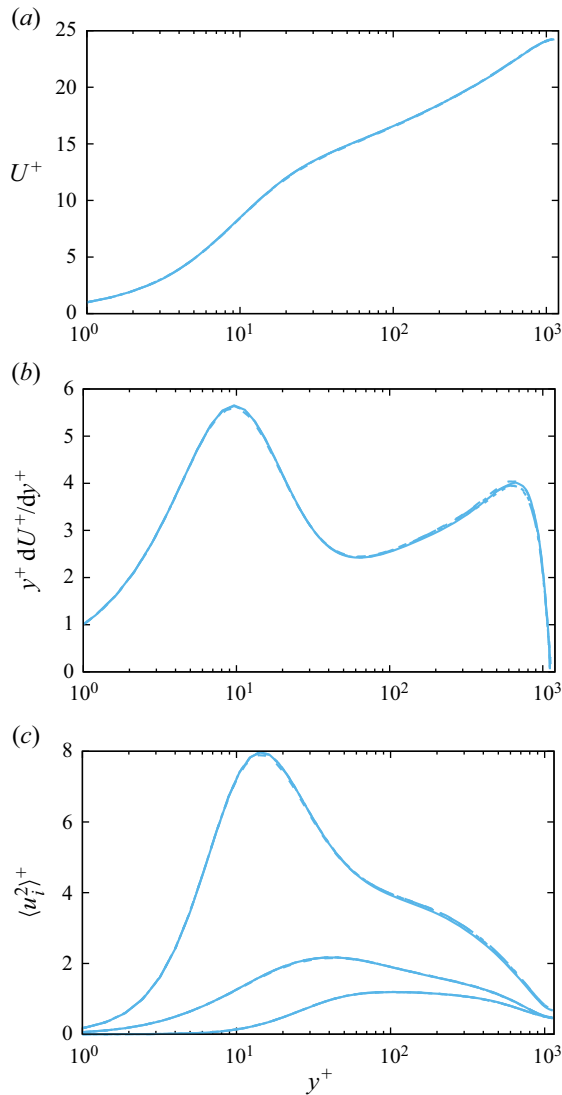


Figure 11. Box and grid sensitivity study for one-point statistics: (a) inner-scaled mean velocity profiles and streamwise velocity variances, (b) log-law diagnostics function, (c) velocity variances. Flow cases C, C-FY, C-L, C-LL are shown, see table 1 for the line style.

profiles tend to cluster around a common logarithmic distribution. The DNS velocity profiles for $Re_\tau \geq 10^3$ follow this distribution with deviations of no more than 0.1 inner units from $y^+ \approx 30$ to $y/R \approx 0.15$, where the core region develops.

Appendix C. Comparison with DNS of channel flow

In figure 14, we present the spanwise spectra of the streamwise velocity obtained from the channel flow DNS conducted by Lee & Moser (2015), at several off-wall locations, while maintaining a constant y^+ . This figure offers clear evidence that universality of the spectra at small scales is achieved when inner scaling is employed, at least for $Re_\tau \gtrsim 2000$. Furthermore, this universal inner-scaled layer tends to become more extended towards

Streamwise velocity variance asymptotics

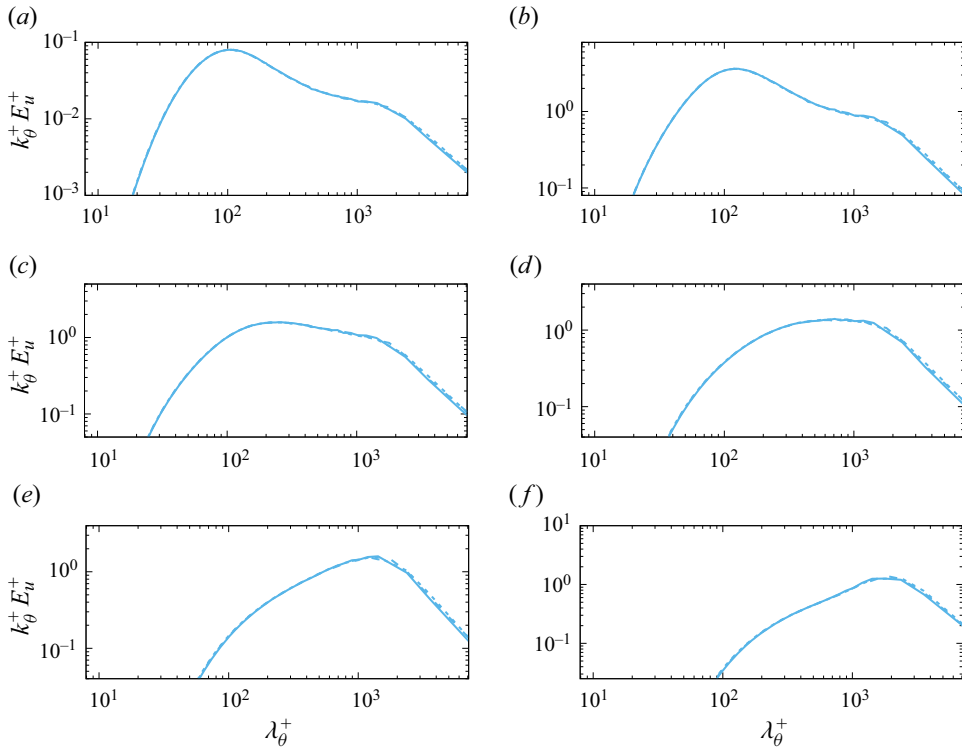


Figure 12. Box and grid sensitivity study for pre-multiplied spanwise spectral densities of streamwise velocity at various wall distances: $y^+ = 1$ (a), $y^+ = 15$ (b), $y^+ = 50$ (c), $y^+ = 100$ (d), $y^+ = 200$ (e), $y^+ = 400$ (f). Flow cases C, C-FY, C-L, C-LL are shown, see table 1 for the line style.

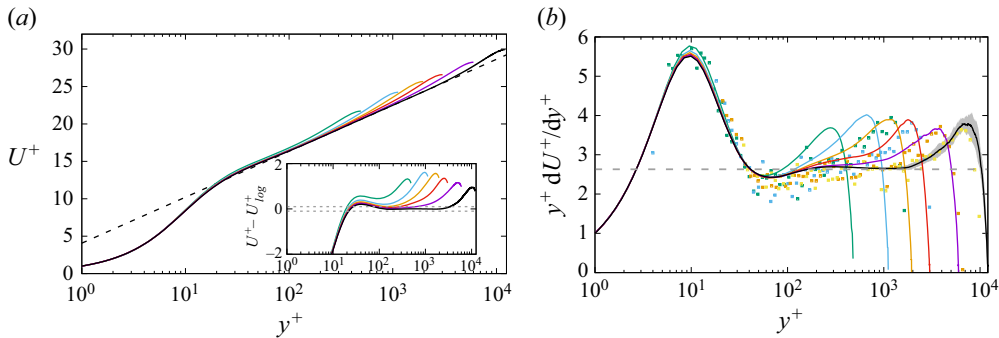


Figure 13. Inner-scaled mean velocity profiles obtained from DNS are presented in panel (a), along with the corresponding log-law diagnostic function shown in panel (b). In panel (a), the dashed line represents the logarithmic fit $U_{\log}^+ = \log y^+ / 0.38 + 4.3$. In panel (b), the dashed horizontal line denotes the inverse of the expected Kármán constant, $\kappa = 0.38$, while symbols denote Princeton SuperPipe data (McKeon, Zagarola & Smits 2005) at $Re_\tau = 1825, 3328, 6617, 10914$. The shaded grey regions denote the expected range of uncertainty for flow case G (not visible in panel (a)). Colour codes for the lines are as described in table 1.

longer wavelengths as Re_τ increases, until a transition to an h -scaled spectral range occurs. These distributions support the findings reported in figure 3, indicating that the pre-multiplied spectra at all considered wall distances exhibit a negative power-law range, with an exponent of approximately 0.18, as for pipe flow. However, due to the more limited range of available Reynolds numbers, a clear power-law behaviour is visible

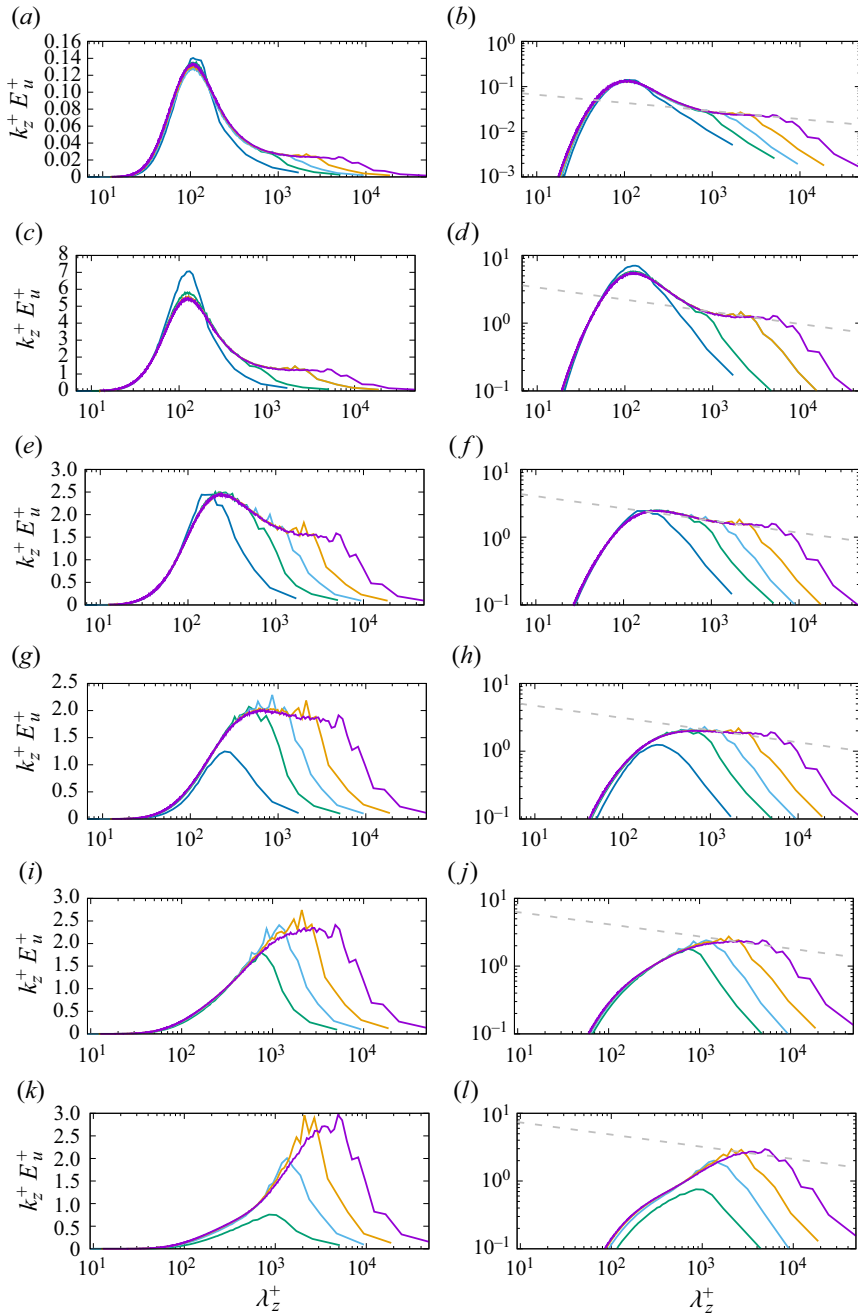


Figure 14. Pre-multiplied spanwise spectral densities of streamwise velocity from DNS of channel flow (Lee & Moser 2015), at various wall distances: $y^+ = 1$ (a,b), $y^+ = 15$ (c,d), $y^+ = 50$ (e,f), $y^+ = 100$ (g,h), $y^+ = 200$ (i,j), $y^+ = 400$ (k,l). A semi-log representation is used in the left-hand side panels, and a log-log representation is used in the right-hand side panels. The dashed grey lines in the right-hand side panels mark the trend $\lambda_0^{-0.18}$. The colour codes correspond to Reynolds numbers $Re_\tau = 180$ (blue), 550 (green), 1000 (cyan), 2000 (orange), 5200 (purple).

Streamwise velocity variance asymptotics

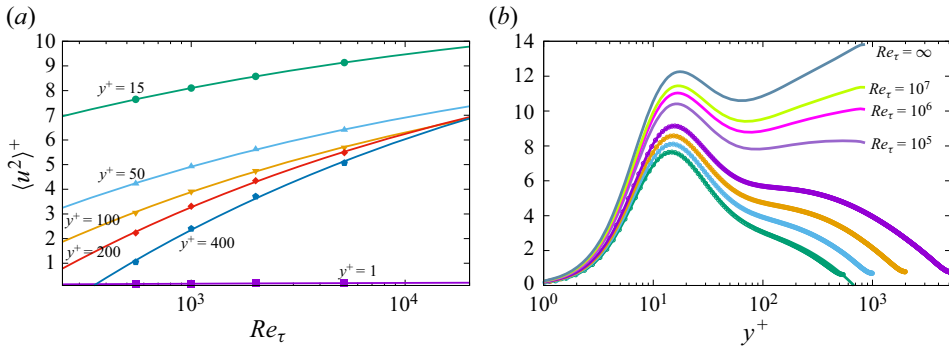


Figure 15. Analysis of velocity variance for turbulent channel flow (Lee & Moser 2015). (a) Streamwise velocity variances (symbols) as a function of Re_τ at various off-wall positions, along with corresponding fits according to (5.5); and (b) predicted wall-normal distributions of streamwise velocity variances at various Re_τ , again according to (5.5). In panel (b), the symbols denote the DNS data used to determine the fit coefficients $A(y^+)$ and $B(y^+)$, with colour codes corresponding to $Re_\tau = 550$ (green), 1000 (cyan), 2000 (orange) and 5200 (purple).

only up to $y^+ \approx 100$. Similar to our analysis for pipe flow, figure 15(a) illustrates the Reynolds-number trends of the velocity variance at various distances from the wall. This figure reaffirms the accuracy of (5.5) in fitting the DNS data and visually highlights deviations from a logarithmic behaviour.

Figure 15(b) depicts the resulting extrapolated distributions at extreme Reynolds numbers. The outcome is qualitatively very similar to that shown in figure 7 for pipe flow, demonstrating saturation of the buffer-layer peak and the onset of a dominant outer-layer peak. We estimate that the asymptotic value of the buffer-layer peak is approximately 12.3, while the wall dissipation should asymptote to about 0.27, which aligns well with the numerical values determined for pipe flow.

REFERENCES

- AFZAL, N. & YAJNIK, K. 1973 Analysis of turbulent pipe and channel flows at moderately large Reynolds number. *J. Fluid Mech.* **61**, 23–31.
- BAARS, W.J. & MARUSIC, I. 2020a Data-driven decomposition of the streamwise turbulence kinetic energy in boundary layers. Part 1. Energy spectra. *J. Fluid Mech.* **882**, A25.
- BAARS, W.J. & MARUSIC, I. 2020b Data-driven decomposition of the streamwise turbulence kinetic energy in boundary layers. Part 2. Integrated energy and. *J. Fluid Mech.* **882**, A26.
- BRADSHAW, P. 1967 ‘Inactive’ motion and pressure fluctuations in turbulent boundary layers. *J. Fluid Mech.* **30**, 241–258.
- CHEN, X. & SREENIVASAN, K.R. 2021 Reynolds number scaling of the peak turbulence intensity in wall flows. *J. Fluid Mech.* **908**, R3.
- CHEN, X. & SREENIVASAN, K.R. 2022 Law of bounded dissipation and its consequences in turbulent wall flows. *J. Fluid Mech.* **933**, A20.
- DEGRAAFF, D.B. & EATON, J.K. 2000 Reynolds-number scaling of the flat-plate turbulent boundary layer. *J. Fluid Mech.* **422**, 319–346.
- HELLSTRÖM, L.H.O. & SMITS, A.J. 2014 The energetic motions in turbulent pipe flow. *Phys. Fluids* **26**, 125102.
- HOYAS, S. & JIMÉNEZ, J. 2006 Scaling of velocity fluctuations in turbulent channels up to $Re_\tau = 2003$. *Phys. Fluids* **18**, 011702.
- HOYAS, S., OBERLACK, M., ALCÁNTARA-ÁVILA, F., KRAHEBERGER, A.V. & LAUX, J. 2022 Wall turbulence at high friction Reynolds numbers. *Phys. Rev. Fluids* **7** (7), 014602.
- HOYAS, S., VINUESA, R., BAXERRES, V. & NAGIB, H. 2024 Resolution and convergence requirements for extended overlap region in wall-bounded turbulence. *Phys. Rev. Fluids* (submitted). [arXiv:2311.05204](https://arxiv.org/abs/2311.05204).

- HULTMARK, M., VALLIKIVI, M., BAILEY, S.C.C. & SMITS, A.J. 2012 Turbulent pipe flow at extreme Reynolds numbers. *Phys. Rev. Lett.* **108**, 094501.
- HUTCHINS, N. & MARUSIC, I. 2007a Evidence of very long meandering features in the logarithmic region of turbulent boundary layers. *J. Fluid Mech.* **579**, 1–28.
- HUTCHINS, N. & MARUSIC, I. 2007b Large-scale influences in near-wall turbulence. *Phil. Trans. R. Soc. Lond. A* **365**, 647–664.
- HWANG, Y. 2015 Statistical structure of self-sustaining attached eddies in turbulent channel flow. *J. Fluid Mech.* **767**, 254–289.
- HWANG, Y. 2016 Mesolayer of attached eddies in turbulent channel flow. *Phys. Rev. Fluids* **1**, 064401.
- HWANG, Y. 2024 Near-wall turbulence intensity as $Re \rightarrow \infty$. *Phys. Rev. Fluids* **2**, 044601.
- JIMÉNEZ, J. & MOSER, R.D. 2007 What are we learning from simulating wall turbulence? *Phil. Trans. R. Soc. Lond. A* **365**, 715–732.
- KIM, K.C. & ADRIAN, R.J. 1999 Very large-scale motion in the outer layer. *Phys. Fluids* **11**, 417–422.
- KLEWICKI, J.C. 2022 Bounded dissipation predicts finite asymptotic state of near-wall turbulence. *J. Fluid Mech.* **940**, F1.
- LEE, M. & MOSER, R.D. 2015 Direct simulation of turbulent channel flow layer up to $Re_\tau = 5200$. *J. Fluid Mech.* **774**, 395–415.
- LENAERS, P., LI, Q., BRETHOUWER, G., SCHLATTER, P. & ÖRLÜ, R. 2012 Rare backflow and extreme wall-normal velocity fluctuations in near-wall turbulence. *Phys. Fluids* **24**, 035110.
- LUCHINI, P. 2017 Universality of the turbulent velocity profile. *Phys. Rev. Lett.* **118** (22), 224501.
- MARUSIC, I. 2001 On the role of large-scale structures in wall turbulence. *Phys. Fluids* **13**, 735–743.
- MARUSIC, I., BAARS, W.J. & HUTCHINS, N. 2017 Scaling of the streamwise turbulence intensity in the context of inner-outer interactions in wall turbulence. *Phys. Rev. Fluids* **2**, 100502.
- MARUSIC, I. & MONTY, J.P. 2019 Attached eddy model of wall turbulence. *Annu. Rev. Fluid Mech.* **51**, 49–74.
- MATHIS, R., HUTCHINS, N. & MARUSIC, I. 2009 Large-scale amplitude modulation of the small-scale structures in turbulent boundary layers. *J. Fluid Mech.* **628**, 311–337.
- MCKEON, B.J., ZAGAROLA, M.V. & SMITS, A.J. 2005 A new friction factor relationship for fully developed pipe flow. *J. Fluid Mech.* **538**, 429–443.
- MENEVEAU, C. & MARUSIC, I. 2013 Generalized logarithmic law for high-order moments in turbulent boundary layers. *J. Fluid Mech.* **719**, R1.
- METZGER, M.M. & KLEWICKI, J.C. 2001 A comparative study of near-wall turbulence in high and low Reynolds number boundary layers. *Phys. Fluids* **13**, 692–701.
- MILLIKAN, C.B. 1938 A critical discussion of turbulent flows in channels and circular tubes. In *Proceedings of the Fifth International Congress for Applied Mechanics, New York* (ed. J.P. Den Hartog & H. Peters), pp. 386–392. Wiley.
- MONKEWITZ, P.A. 2021 The late start of the mean velocity overlap log law at $y^+ = O(10^3)$ – a generic feature of turbulent wall layers in ducts. *J. Fluid Mech.* **910**, A45.
- MONKEWITZ, P.A. 2022 Asymptotics of streamwise Reynolds stress in wall turbulence. *J. Fluid Mech.* **931**, A18.
- MONKEWITZ, P.A. 2023 Reynolds number scaling and inner-outer overlap of stream-wise Reynolds stress in wall turbulence. [arXiv:2307.00612](https://arxiv.org/abs/2307.00612).
- MONKEWITZ, P.A. & NAGIB, H.M. 2015 Large-Reynolds-number asymptotics of the streamwise normal stress in zero-pressure-gradient turbulent boundary layers. *J. Fluid Mech.* **783**, 474–503.
- NAGIB, H., MONKEWITZ, P. & SREENIVASAN, K. 2024 Reynolds number required to accurately discriminate between proposed trends of peak normal stress in wall turbulence. *Phys. Rev. Fluids* (submitted). [arXiv:2312.01184](https://arxiv.org/abs/2312.01184).
- ONO, M., FURUICHI, N. & TSUJI, Y. 2023 Reynolds number dependence of turbulent kinetic energy and energy balance of 3-component turbulence intensity in a pipe flow. *J. Fluid Mech.* **975**, A9.
- PERRY, A.E. & CHONG, M.S. 1982 On the mechanism of wall turbulence. *J. Fluid Mech.* **119**, 173–217.
- PERRY, A.E., HENBEST, S. & CHONG, M.S. 1986 A theoretical and experimental study of wall turbulence. *J. Fluid Mech.* **165**, 163–199.
- PERRY, A.E. & MARUSIC, I. 1995 A wall-wake model for the turbulence structure of boundary layers. Part 1. Extension of the attached eddy hypothesis. *J. Fluid Mech.* **298**, 361.
- PIROZZOLI, S. & ORLANDI, P. 2021 Natural grid stretching for DNS of wall-bounded flows. *J. Comput. Phys.* **439**, 110408.
- PIROZZOLI, S., ROMERO, J., FATICA, M., VERZICCO, R. & ORLANDI, P. 2021 One-point statistics for turbulent pipe flow up to $Re_\tau \approx 6000$. *J. Fluid Mech.* **926**, A28.

Streamwise velocity variance asymptotics

- PRANDTL, L. 1925 Bericht über Untersuchungen zur ausgebildeten Turbulenz. *Z. Angew. Math. Mech.* **5**, 136–139.
- RUSO, S. & LUCHINI, P. 2017 A fast algorithm for the estimation of statistical error in DNS (or experimental) time averages. *J. Comput. Phys.* **347**, 328–340.
- SCHLICHTING, H. & GERSTEN, K. 2000 *Boundary layer theory*, 8th edn. Springer.
- SPALART, P.R. 1988 Direct numerical simulation of a turbulent boundary layer up to $Re_\theta = 1410$. *J. Fluid Mech.* **187**, 61–98.
- SREENIVASAN, K.R. 1989 The turbulent boundary layer. In *Frontiers in Experimental Fluid Mechanics* (ed. M. Gad-el-Hak), pp. 159–209. Springer.
- TOWNSEND, A.A. 1976 *The Structure of Turbulent Shear Flow*, 2nd edn. Cambridge University Press.
- VALLIKIVI, M., GANAPATHISUBRAMANI, B. & SMITS, A.J. 2015 Spectral scaling in boundary layers and pipes at very high Reynolds numbers. *J. Fluid Mech.* **771**, 303–326.
- WILLERT, C.E., SORIA, J., STANISLAS, M., KLINNER, J., AMILI, O., EISELDER, M., CUVIER, C., BELLANI, G., FIORINI, T. & TALAMELLI, A. 2017 Near-wall statistics of a turbulent pipe flow at shear Reynolds numbers up to 40 000. *J. Fluid Mech.* **826**, R5.